

## Invited research article

# Magnetic fabric of Bengal fan sediments: Holocene record of sedimentary processes and turbidite activity from the Ganges-Brahmaputra river system



Eva Moreno<sup>a,\*</sup>, Fabien Caroir<sup>b</sup>, Lea Fournier<sup>c</sup>, Kelly Fauquembergue<sup>c</sup>, Sébastien Zaragosi<sup>c</sup>, Ronan Joussain<sup>d</sup>, Christophe Colin<sup>d</sup>, Marie-Madeleine Blanc-Valleron<sup>e</sup>, François Baudin<sup>f</sup>, Thibault de Garidel-Thoron<sup>g</sup>, Jean Pierre Valet<sup>h</sup>, Franck Bassinot<sup>i</sup>

<sup>a</sup> Laboratoire d'Océanographie et du Climat: Expérimentations et approches numériques, UMR 7159 CNRS, IRD, Sorbonne Université/MNHN/IPSL, Boîte 100 - 4, place Jussieu, 75252 Paris cedex 05, France

<sup>b</sup> UMR 8187, LOG, Laboratoire d'Océanologie et de Géosciences, Université Lille, CNRS, Université Littoral Côte d'Opale, F 59000 Lille, France

<sup>c</sup> UMR CNRS 5805 EPOC, OASU, Université de Bordeaux, Allée Geoffroy Saint-Hilaire - CS 50023, 33615 Pessac cedex, France

<sup>d</sup> CNRS, GEOPS, Université Paris-Saclay, 91405, Orsay, France

<sup>e</sup> CR2P, UMR 7207, Muséum National d'Histoire Naturelle, 43 Rue Buffon - CP38, Paris, France

<sup>f</sup> ISTE - Institut des Sciences de la Terre Paris, Sorbonne Université, 4 place Jussieu, CP 117, 75005 Paris, France

<sup>g</sup> CNRS, IRD, Coll. de France, INRAE, CEREGE, Aix-Marseille Université, Technopôle de l'Arbois - BP80, 13545 Aix-en-Provence cedex 04, France

<sup>h</sup> Institut De Physique Du Globe De Paris, 1, Université de Paris, 1 rue Jussieu, 75238 Paris cedex 05, France

<sup>i</sup> Laboratoire des Sciences du Climat et de l'Environnement, LSCE/IPSL, CEA-CNRS-UVSQ, Université Paris-Saclay, F-91191 Gif-sur-Yvette, France

## ARTICLE INFO

## Keywords:

Bengal fan  
Holocene  
Turbidite activity  
Magnetic fabric  
Magnetic mineralogy

## ABSTRACT

We present here a study based on the Anisotropy of Magnetic Susceptibility (AMS) and magnetic mineralogy carried out on the composite core MD17&18 taken from the eastern levee of the active channel of the middle Bengal Fan in the Indian Ocean. Based on C-14 dating, the sedimentary sequence covers 9.8 ka in 39 m of sediment. It therefore records at very high resolution the variations in continental material exported to the ocean by the Ganges-Brahmaputra river system during the Holocene.

This sequence was divided into two units according to turbidite activity: Unit 1 from 9.8 to 9.2 ka cal. BP representing 39 m of coarse-grained turbidite sequences (coarse silts to fine sands) and extremely high sedimentation rates. Unit 2 of 9.2 ka cal. BP to the present characterized by a sharp decrease in the sedimentation rate, the presence of fine-grained turbidites characterized by strong decrease in the ln(Ti/Ca) ratio.

Our AMS results indicate that the magnetic fabric is highly sensitive to the mode of deposition. The turbidite sequences are clearly characterized by very high F and Pj values, not only of the coarse-grained turbidite levels in unit 1, but also of the fine turbidites in unit 2. We suggest that this strong degree of anisotropy is the result of the strong and rapid deposition during the turbidite sequences which induces an additional compaction effect.

Furthermore, low temperature SIRM measurements revealed that the magnetic minerals representative of the Ganges and Brahmaputra drainage area are magnetite, hematite and goethite. A higher supply in fine-grained magnetite was observed during the turbidite sequences in phase with an increase in sediment grain size.

## 1. Introduction

The anisotropy of magnetic susceptibility (AMS) technique is a useful method to study the sedimentary fabric of marine and lakes sediment. Magnetic fabric derived from AMS analyses reflect the shape and preferred alignment of sedimentary particles during deposition under the presence of bottom-currents. Therefore, AMS has been successfully used to identify bottom currents directions in different environments including contourites, submarine fan, fluvial and delta

environment (Abdeldayem, 1999; Beckers et al., 2016; Felletti et al., 2016; Ge et al., 2012; Kissel et al., 1998; Parés et al., 2007; Tamaki et al., 2015). The AMS technique is particularly powerful in combination with grain-size measurements as these two properties enable to differentiate between high depositional energy environments like turbidite or mass-transport deposits composed of coarse to fine-grained terrigenous detritus and hemipelagic deposits built by settling (Abdeldayem, 1999; Joseph et al., 1998; Kissel et al., 1997; Kissel et al., 1998; Meissl et al., 2011). These techniques have also been successfully

\* Corresponding author.

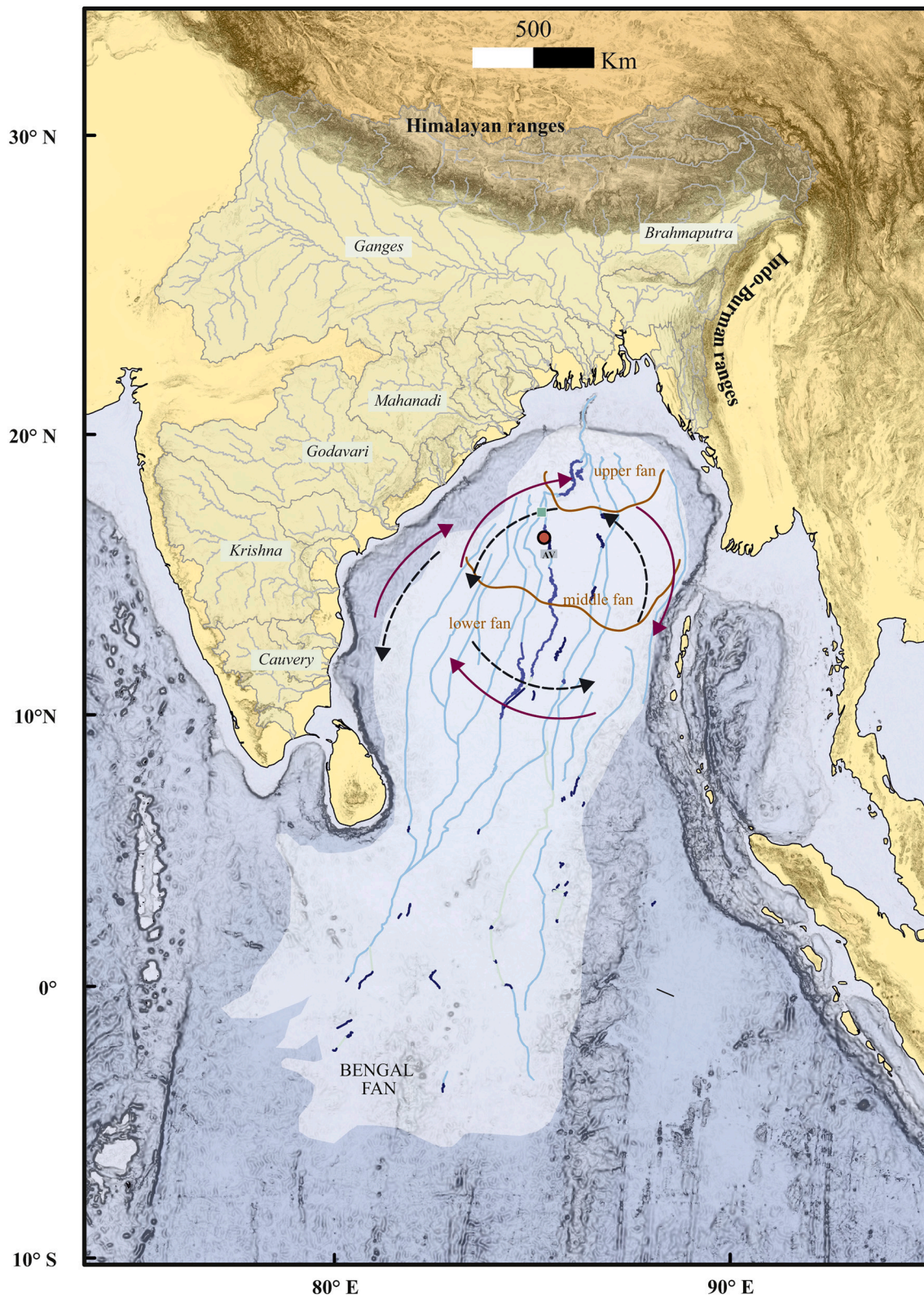
E-mail address: [eva.moreno@mnhn.fr](mailto:eva.moreno@mnhn.fr) (E. Moreno).

<https://doi.org/10.1016/j.margeo.2020.106347>

Received 22 May 2020; Received in revised form 8 September 2020; Accepted 15 September 2020

Available online 22 September 2020

0025-3227/ © 2020 Elsevier B.V. All rights reserved.



- MD17&18 (This study)
- MD161/29 (Volvoikar et al. 2020)
- AV Active valley
- ➔ Southwest Monsoon
- - ➔ Northeast Monsoon

(caption on next page)

**Fig. 1.** Location map from of cores MD12-3417 and MD12-3418CQ (composite core MD17&18) and core MD161/29 (Volvoikar et al., 2020) mentioned in this article. The map shows the physiography of the Ganges-Brahmaputra sedimentary system, from the catchment to the deep-sea fan (Fauquembergue et al., 2019). Fluvial systems are in light to dark blue (Curry et al., 2003; Kolla et al., 2012; Schwenk et al., 2003; Thomas et al., 2012; Thu et al., 2001; Weber et al., 2003). AV is the most recently active valley. The arrows indicate the surface current during southwest and northeast monsoon (Sun et al., 2019). (For interpretation of the references to colour in this figure legend, the reader is referred to the web version of this article.)

used to identify major seismic events in lake (Carrillo et al., 2008) and marine environments (Campos et al., 2014; Campos et al., 2013).

In this article we study the magnetic fabrics of Holocene sediments located on the eastern levee of the Bengal Fan Active Channel that have recorded several turbidite deposits (Fig. 1). This channel is fed by the Ganges-Brahmaputra (G-B) river system and has been subjected to intense turbidite activity for the past 14.5 ka cal. BP (Weber et al., 1997). Here we focus on a continuous and unique core recording more than 200 silty-sandy to fine silt turbidity sequences that have been deposited during the past 9.8 ka cal. BP under extremely high sedimentation rates (Fournier et al., 2017). The aim of this work is to: (1) investigate the anisotropy of magnetic susceptibility (AMS) at high resolution; (2) search for consistent trends in the AMS properties of the levee turbidites; (3) determine the relationship of the magnetic fabric with the grain-size and the mineralogical properties of previously studied turbidite layers (Fournier et al., 2017).

## 2. Geological setting of the Bengal Fan

The Bengal Fan is the largest submarine fan in the world, with a length of about 3000 km, a width of about 1000 km and a thickness that can reach 16.5 km (Curry et al., 2003). Terrigenous material is mainly supplied by the G-B Rivers (Curry et al., 2003) with minor contributions from other rivers in Bangladesh, India and Burma (Liu et al., 2019b). The annual sedimentary discharges of the G-B Rivers are estimated at around  $1 \times 10^9$  t/y which is the largest of the world (Milliman, 2001). However, the hydrological cycle in the G-B basin is governed by the summer monsoon and consequently, the river runoff in the G-B is highly seasonal: about 90% of Ganges sediments and more than 80% of Brahmaputra sediments are transferred from June to September (Unger et al., 2003).

Riverine sediments are transferred to the deep-sea fan as turbidity currents in channel-levee systems that have been developed from G-B river mouth to the equatorial sea area. This turbidite system is known as the Bengal Fan (Curry et al., 2003). Nowadays, there is only one active channel connected by the submarine canyon “Swath of No Ground” (SoNG) (Fig. 1) (Curry et al., 2003).

The construction of this channel began around 14.5 ka cal. BP (Weber et al., 1997) and was followed by intense turbidite activity up to 9.2 ka cal. BP which resulted in large sediment thickness. Thus, at the site of the MD12-3417 and MD12-3418 cores that will be studied in this work, the sedimentation rate between 9.8 and 9.2 ka cal. BP was unusually high, between 3.5 and 9.5 cm/year due to almost continuous turbidite inputs. This turbidite activity continued during the sea level rise and in the rest of the Holocene but in a less intense way so that the sedimentation rate was reduced to 0.02–0.18 cm/year from 9.2 ka cal. BP, being still very high (Fournier et al., 2017).

Two main processes have been documented to influence the construction of the SoNG system: post-glacial sea-level forcing and hydrological forcing through the monsoon. According to previous works (Fauquembergue et al., 2019; Fournier et al., 2017; Jousain et al., 2017; Weber et al., 1997), turbidite sedimentation in the Active Channel was clearly linked with global sea-level rise in presence of higher precipitation related to an enhancement of the Indian summer monsoon during early Holocene. The global sea level from 14.5 to 9.2 ka cal. BP is between –95 and –20 m with respect to present day according to the global sea-level curve (Lambeck et al., 2014). As consequence, there was good a fluvial connection with the SoNG leading to sediments largely bypassing both delta and shelf margin and

being exported to the Bengal Fan. Additionally, Indian monsoon precipitation fluctuated significantly during the Holocene. Numerous studies showed that the Indian summer monsoon was strengthened during the early Holocene (Gupta et al., 2005; Jousain et al., 2017; Kumar et al., 2019; Thamban et al., 2007) followed by a gradual weakening over the past 8 ka with a more or less stable dry phase beginning ~5 ka BP that coincides with the onset of an arid Indian phase (Sharma et al., 2004). As a result, the G-B sediment discharge was enormously increased during early Holocene (Goodbred and Kuehl, 2000). Results estimated that the mean sediment load of the G-B river system was 2 times higher ( $\sim 2.3 \times 10^9$  t/year) between 11 and 7 ka cal. BP, than for present time (Goodbred and Kuehl, 2000).

## 3. Studied cores and previous works

Calypso giant-piston core MD12-3417 (16°30.03'N; 87°47.82'E; water depth: 2564 m, 39.77 m long) and the Calypso square (CASQ) gravity core MD12-3418CQ located at the same site (16°30.27'N; 87°47.92'E; water depth: 2557 m, 8.52 m long) were taken during the MD191/MONOPOL expedition (Bassinot and Beaufort, 2012) of the French R/V Marion Dufresne in 2012 (Fig. 1). The cores are stored in the marine collection of the *Museum national d'Histoire naturelle* from Paris (France) under the inventory numbers MNHN-GS-MD12-3417 and MNHN-GS-MD123418CQ.

These cores were taken on the eastern levee of the active channel. Two previous studies of these cores have been already conducted to constrain the controlling factors implied in turbidite activity of the active channel (Fournier et al., 2017) and the link between Indian summer monsoon rainfall intensity and weathering of the G-B river basin (Jousain et al., 2017) during the Holocene.

Fournier et al. (2017) used a composite record, generated by splicing core MD12-3418CQ with the base of core MD12-3417 (11–40 m). This composite record was achieved by matching the X-ray fluorescence (XRF) high-resolution data of both cores and then converting core MD12-3417 depth scale into core MD12-3418CQ depth scale. This composite record will be subsequently referred to MD17&18. Based on thirteen  $^{14}\text{C}$  dates (Fournier et al., 2017), the composite core MD17&18 represents a continuous sedimentary record for the past 9.8 ka cal. BP (Fig. 2).

## 4. Sampling and methods

### 4.1. Anisotropy of magnetic anisotropy (AMS)

AMS measurements were carried out at the *Institut de Physique du Globe* (IPGP) in Paris using an AGICO Kappabridge KLY3 susceptibilimeter (with  $2 \times 10^{-8}$  SI sensitivity) and an alternating field of 300  $\text{Am}^{-1}$  intensity at 875 Hz frequency.

A total of 565 discrete samples were obtained through continuous sub-sampling by pressing 8  $\text{cm}^3$  plastic cubes. All samples from the MD12-3417 core were taken from the working halves. The cubes were oriented along the Z axis of the core with the arrow pointing to the top of the section. The average sampling interval is 5 cm, varying from a maximum of 20 cm in the hemipelagic sediment to a minimum of 2 cm in turbidite sequences. Core CASQ MD12-3418 core has a square section ( $0.25 \times 0.25 \text{ m}^2$ ). The sediment was first sub-sampled on-board in 5 equivalent “half-sections” using PVC U-channels 6 cm wide and 5 cm deep. The cubes for the AMS were then taken in one of these 5 “half-sections” and oriented in the same way as for the MD12-3417 core.

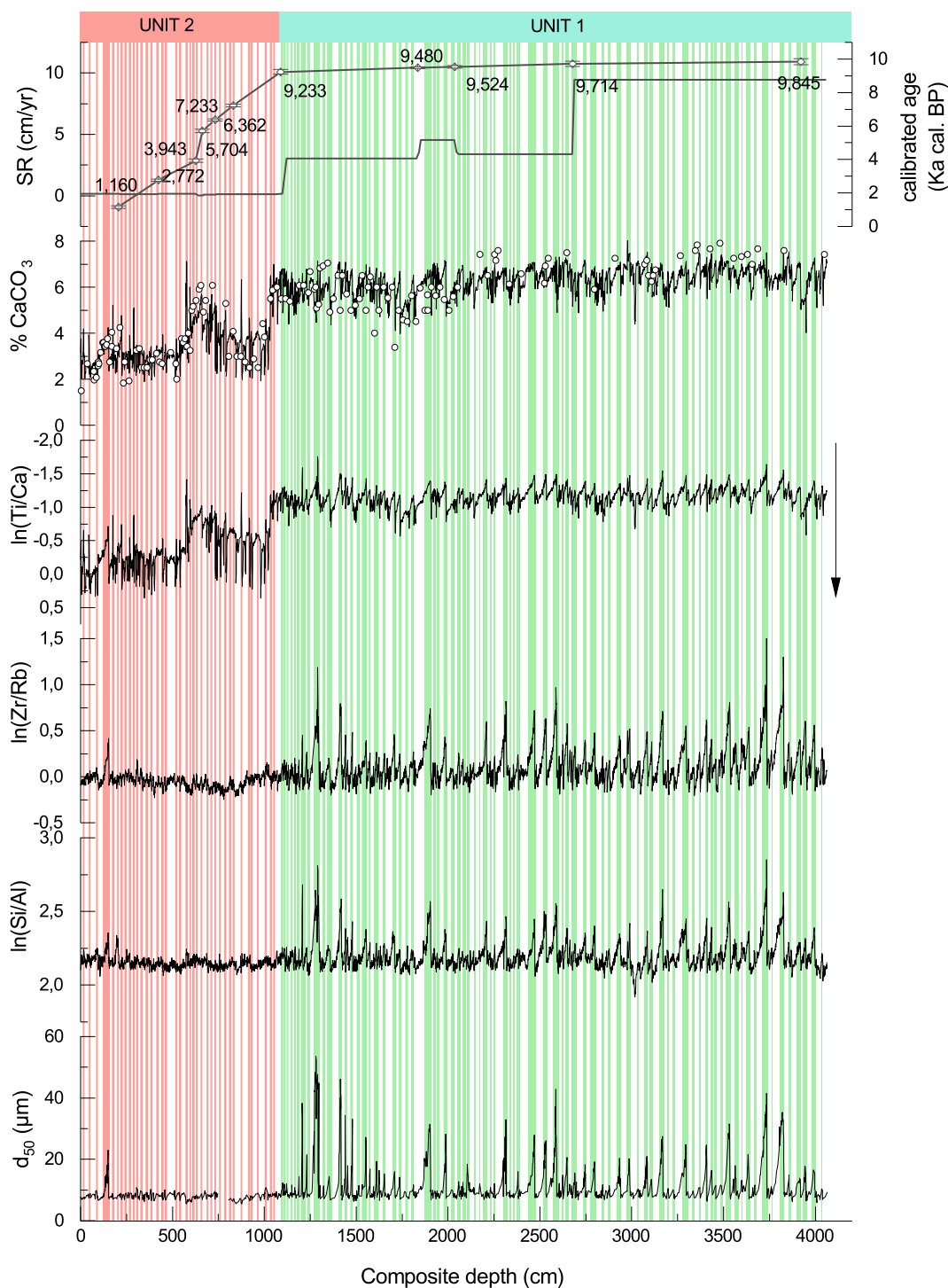


**Fig. 2.** : From top to the bottom: the sedimentation rate and AMS  $^{14}\text{C}$  ages; calcium carbonate contents (%  $\text{CaCO}_3$ ) measured using a carbonate bomb and rock-eval measurements (white dots) and calibrated from XRF-Ca counts (line);  $\ln(\text{Ti}/\text{Ca})$  (inversed scale),  $\ln(\text{Zr}/\text{Rb})$  and  $\ln(\text{Si}/\text{Al})$  ratios measured by XRF; and  $d_{50}$  (median value in  $\mu\text{m}$  of the particle size distribution) estimated from laser granulometry. Age mode, XRF-Ti/Ca and Zr/Rb ratios and grain-size data were already published (Fournier et al., 2017) while the Si/Al ratio is published now for the first time. Depths are composite depths (cm) of core MD17&18. Recognized Units 1 and 2 are indicated on the top. Turbidite levels are indicated in green (Unit 1) and red (Unit 2). (For interpretation of the references to colour in this figure legend, the reader is referred to the web version of this article.)

The AMS is determined from a second order symmetric tensor. The Eigen vectors define the maximum ( $K_1$ ), intermediate ( $K_2$ ) and minimum ( $K_3$ ) axes of the susceptibility ellipsoid that represents the global anisotropy resulting from the individual grain shapes and their alignment within the sample. It depends also on the crystallographic axes (Tarling and Hrouda, 1993).

The magnetic lineation ( $K_1/K_2$ ) and magnetic foliation ( $K_2/K_3$ ) have been used to describe the magnetic fabric. The term magnetic lineation (L) may be used to characterize the intensity of the linear-parallel orientation, while the magnetic foliation (F) characterizes the intensity of the planar-parallel orientation of minerals in a rock (Tarling and Hrouda, 1993). When plotted on Flinn diagrams they enable to

determine whether the fabric is oblate ( $F > L$ ) or prolate ( $F < L$ ). The shape parameter  $T$  ( $T = [2\eta_2 - \eta_1 - \eta_3]/(\eta_1 - \eta_3)$ ) fluctuates between 1 and  $-1$ . When  $T$  is close to 1 or positive, the ellipsoid is oblate, when  $T$  is negative, then the ellipsoid is prolate. If  $T = 0$ , then the ellipsoid is neutral or spherical. The  $P_j$  parameter defines the corrected degree of anisotropy, indicates the intensity of the preferred orientation of magnetic minerals in a rock, high values represent a strong degree of anisotropy ( $P_j = \exp.\sqrt{2[(\eta_1 - \eta_m)^2 + (\eta_2 - \eta_m)^2 + (\eta_3 - \eta_m)^2]}$ ) with  $\eta_1 = \ln K_1$ ;  $\eta_2 = \ln K_2$ ;  $\eta_3 = \ln K_3$  and  $\eta_m = \sqrt[3]{\eta_1 \cdot \eta_2 \cdot \eta_3}$ . Lastly, we used the inclination of the  $K_3$  direction ( $\text{In}K_3$ ) which indicates the tilt of the short axis  $K_3$ .

#### 4.1.1. Anhyseretic Remanent Magnetization (ARM)

In addition, the Anhyseretic Remanent Magnetization (ARM) was measured on 78 samples between 770 cm and 2051 cm (composite core depth) with a resolution of 5-20 cm depending on the interval. The ARM was imparted in a 50  $\mu\text{T}$  steady field combined with a linearly decaying alternating field of 80 mT using a Schonstedt demagnetizer that was equipped for that purpose.

Following the acquisition, the ARM measurements were performed on a 2G cryogenic magnetometer at the IPGP. Thereafter, ARM results were divided by magnetic susceptibility (ARM/K). Indeed, the ARM/k ratio is inversely related to the grain-size of magnetite and titanomagnetite (Banerjee et al., 1981; King et al., 1982). These results are shown in the complementary Fig. S3 compared with the percentage of sands and silts.

#### 4.2. Low temperature measurements

Low-temperature isothermal remanence magnetizations (LT-SIRM) were made in core MD17&18 using a Quantum Design Magnetic Property Measurement System (MPMS2) SQUID magnetometer at the IPGP in Paris (France). For these analyses, we selected a small amount of sediment (a few milligrams) from the hemipelagic intervals and turbidites of Unit 1 and 2. The sediment was dried, ground and inserted within gelatin capsules for measurements in the MPMS. Two different LT-SIRM experiments were performed.

-Low-temperature (10K) Saturation Isothermal Remanent Magnetization (SIRM) were imparted after cooling in a 2.5 T field (field cooling, FC) and in a zero field environment (zero field cooling, ZFC). The SIRM was measured in approximately zero field at 5-K intervals up to 300 K.

-SIRM magnetization was imparted at room temperature (RT-SIRM) by applying a maximum field of 2.5 T at 300 K followed by continuous cooling in zero field to 10 K and subsequent continuous warming back to 300 K at 5-K intervals.

#### 4.3. Sedimentological analyses

The sedimentological analyses performed include the high resolution analysis of the chemical elements by X-ray fluorescence (XRF) and the analysis of the grain-size and  $\text{CaCO}_3$  content. XRF and grain-size results have already been published in Fournier et al. (2017).

##### 4.3.1. X-ray images, Scopix

X-ray images were taken using the Scopix X-ray imaging system from the PAACS platform at the EPOC laboratory. The acquisition was done on 1 cm thick aluminum plates taken from the core half-sections. This method optimizes the resolution and homogenizes the X-ray response over the entire core.

X-ray radiography makes it possible to observe variations in the density and nature of the sediment. The images obtained are based on a grey scale. Denser sediment tends to absorb more x-rays, resulting in a darker shade of grey. On the contrary, a sediment that is not very dense, or with a coarser grain-size, will give a lighter shade of grey. Thus, this tool makes it possible to visualize the structure and organization of

sediments and to identify sedimentary processes and it can be used to recognize facies such as turbidites (Migeon et al., 1998).

#### 4.3.2. Carbonate content

A total of 148  $\text{CaCO}_3$  analyses were performed using a carbonate bomb at MNHN (50 measurements) and rock-Eval at ISTEf (98 measurements) using a method devoted to recent sediments (Baudin et al., 2015). These data were subsequently used to calibrate the Ca values measured by XRF using a linear equation (Pearson correlation = 0.89), this linear equation was then applied to the continuous XRF record to derive a very high-resolution  $\text{CaCO}_3$  curve.

### 5. Results

#### 5.1. Down-core fluctuations in XRF data and grain-size parameters

Fig. 2 shows the selected geochemical parameters analyzed by XRF together with the  $\text{CaCO}_3$  content and the median grain-size (d50) of the MD17&18 composite core as function of depth. In addition, in this figure, the sedimentation rate and radiocarbon data can also be seen. Age mode, Ti/Ca and Zr/Rb ratios and the d50 data were already published (Fournier et al., 2017). The Si/Al ratio are published now for the first time. In this article, the XRF-ratios were expressed as logarithms of ratios of abundances as they provide the most robust record of relative chemical changes (Weltje and Tjallingii, 2008).

The  $\ln(\text{Zr/Rb})$  ratio (Calvert and Price, 1983; Dypvik and Harris, 2001) and  $\ln(\text{Si/Al})$  ratio (Liu et al., 2018) can be interpreted to indicate grain-size variations. Due to the relative high content of sand and coarse silt within the turbidite layers, water content can increase and reduce element intensities (Boyle et al., 2015), specially for the lighter elements Al and Si (Tjallingii et al., 2007). However, the use of relative variations using element ratio makes it possible to minimize the influence of sediment porosity and water content. In fact, it can be seen in Fig. 2 that the variations of the  $\ln(\text{Zr/Rb})$  and  $\ln(\text{Si/Al})$  ratios are nearly identical to the variations of d50 and that these vary in phase and with similar amplitudes to the grain-size.

Besides, the  $\ln(\text{Ti/Ca})$  ratio is commonly used to compare the siliclastic fraction (Ti) and the biogenic Ca fraction (Kuhnt et al., 2015; Revel et al., 2015; St-Onge et al., 2007). However, in core MD17&18, microscopic observations indicate that  $\text{CaCO}_3$  is mainly composed of detrital calcite (Fournier et al., 2017). Detrital calcite was more concentrated in turbidite sequences and the  $\ln(\text{Ti/Ca})$  ratio was used to identify fine-grained turbidite sequences.

Based on the previous work by Fournier et al. (2017), core MD17&18 was divided in two Units depending on the intensity of turbidite activity:

- Unit 1 that covers the age interval between  $9.862 \pm 2.00$  ka cal. BP and  $9.226 \pm 1.40$  ka cal. BP (1089–4053 cm in composite depth) and includes only core MD12-3417. Several turbidite levels can be easily recognized from the increase in median grain-size,  $\ln(\text{Zr/Rb})$  and  $\ln(\text{Si/Al})$  ratios and the decrease in the  $\ln(\text{Ti/Ca})$  ratio. The  $\text{CaCO}_3$  percentage of the sediment is around 6%.
- Unit 2 goes from  $9.226 \pm 1.40$  ka cal. BP to the present (0–1088 cm) and includes the entire MD12-3418CQ core (0–824 cm) and a small interval of core MD12-3417 (831–1088 cm). In this unit, only one peak is visible in the median grain-size and the  $\ln(\text{Zr/Rb})$  and  $\ln(\text{Si/Al})$  ratios between 120 and 155 cm similarly to those observed in Unit 1. The rest of the interval has a median grain-size of 10  $\mu\text{m}$ . However, several fine-grained turbidites were recognized from the  $\ln(\text{Ti/Ca})$  ratio. The percentage of  $\text{CaCO}_3$  is around 3%.

#### 5.2. Down-core fluctuations in AMS parameters

The down-core fluctuations of bulk magnetic susceptibility ( $K_m$ ),

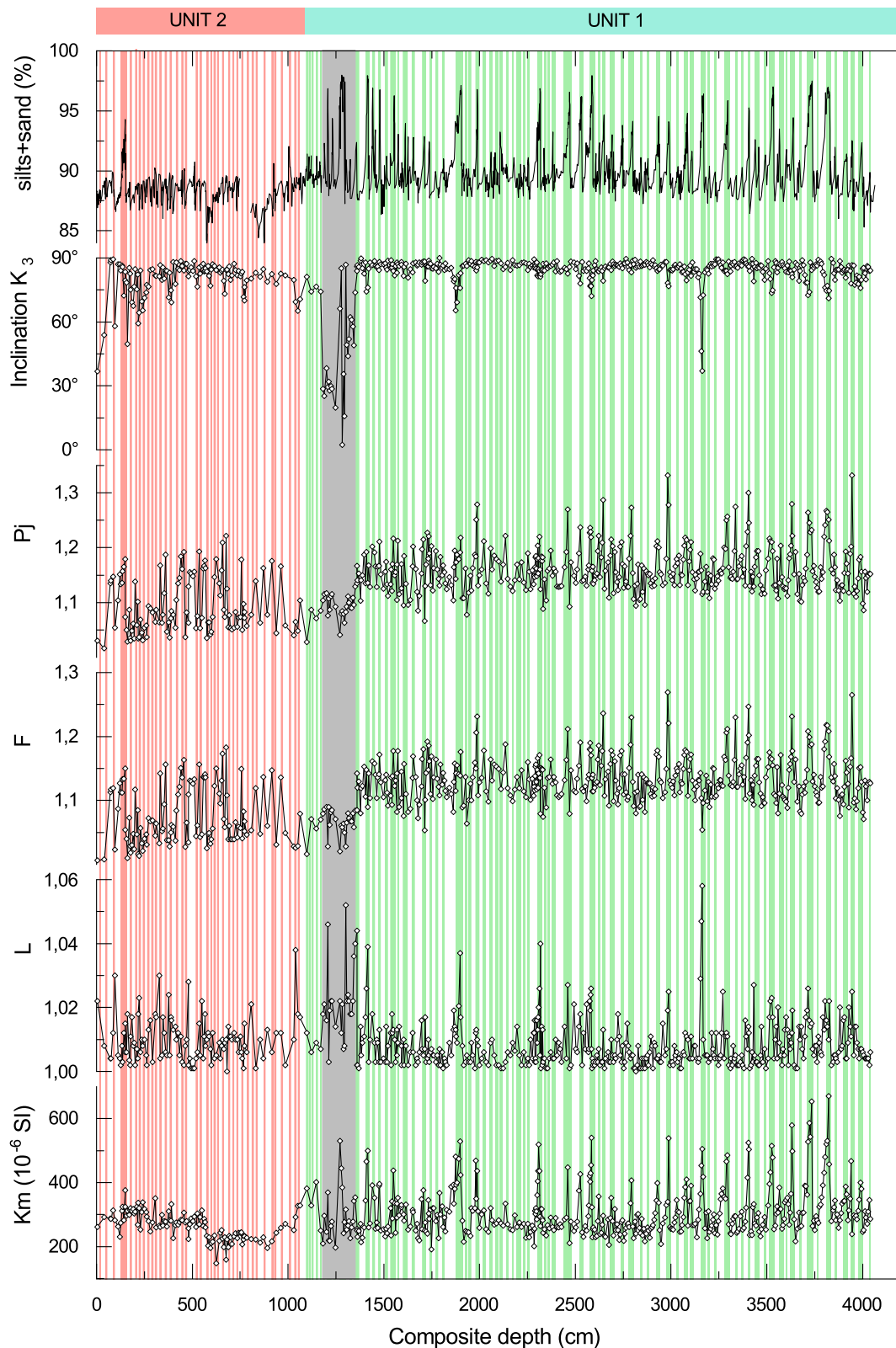


**Fig. 3.** : From top to the bottom: Percentage of silts+sands estimated from grain-size analysis (Fournier et al., 2017);  $\text{Inc}K_3$ ; corrected degree of anisotropy ( $P_j$ ); foliation (F); lineation (L) and magnetic susceptibility measured on cubes. All these parameters were obtained from the anisotropy of magnetic susceptibility measurements. Depths are composite depths (cm). Recognized Units 1 and 2 are indicated on the top. Turbidite levels are indicated in green (Unit 1) and red (Unit 2). The grey band indicates section XI of core MD12-3417 whose structure shows signs of disturbance associated with coring. (For interpretation of the references to colour in this figure legend, the reader is referred to the web version of this article.)

lineation (L), foliation (F), corrected degree of anisotropy (Pj), shape parameter (T), inclination of the AMS  $K_3$  axes and percentage of silts and sands of core MD17&18 have been reported in Fig. 3. The turbidite level between 120 and 155 cm was already studied by AMS in a previous study (Tanty et al., 2016). Additional measurements were performed on new samples.

*Bulk magnetic susceptibility (Km)* is usually considered as a proxy for rock composition. In core MD17&18, Km fluctuated in parallel to the percentage of silts and sands. The Km value of core MD17&18 range between  $100\text{--}700 \times 10^{-6}$  SI. The mean susceptibilities of  $275 \pm 38 \times 10^{-6}$  SI for Unit 1 and  $267 \pm 43 \times 10^{-6}$  SI for Unit 2 outside the turbidite layers are relative similar and they correspond to values of paramagnetic minerals ( $< 300 \times 10^{-6}$ SI) like clays and phyllosilicates (e.g., Tarling and Hrouda, 1993). However, during the turbidite sequences of Unit 1, the Km increase highly, mean values were  $364 \pm 93 \times 10^{-6}$  SI with a maximum of  $671 \times 10^{-6}$  SI which reflect either a stronger magnetic concentration or changes in magnetic mineralogy.

The lineation is very low in the entire record ( $L < 1.06$ ) and shows excursions associated with some but not all the turbidite layers. In Unit 1, the highest L values correspond to either thick turbidite levels or levels with larger sediment grain-size. In Unit 2, many more high L values are characterized by a slight increase in sediment grain-size, except at level 120–155 cm.

Besides, F and Pj are extremely high (up to 1.33 for Pj and to 1.3 for F) and with similar downcore patterns, which indicates that the degree of anisotropy is controlled by foliation. In Unit 1, the values are higher than in Unit 2, but there is no clear increase with depth and therefore compaction has no impact. However, F and Pj show a clear increase in turbidite levels of both Units 1 and 2. In Unit 1, the increase is accompanied by a larger magnetic susceptibility.

The inclination of the  $K_3$  axes is close to  $90^\circ$ , thus, normal to the bedding plane. This corresponds to classic magnetic fabric of sediments that were deposited in still water on an horizontal plane. However, several turbidite layers with lower  $\text{Inc}K_3$  indicate that grains were tilted by more than  $10\text{--}20^\circ$  and even sometimes by more than  $60^\circ$ . The largest deviations ( $\text{Inc} = 60\text{--}75^\circ$ ) were observed between 1180 and 1350 cm (section XI of core MD12-3417). This behavior is not linked to a different deposition mechanism but was rather caused by an important perturbation of the sedimentary structure. Indeed, in this interval, there is one of the thickest turbidites in the core characterized by a very high amount of sand and a high water content. This feature, was likely the cause of non-optimal coring recovery, which disturbed the sedimentary structure and explain the unusual AMS values in section 11 of core MD12-3417. This perturbation is observed in the X-ray photographs (Fig. S2, supplementary data). One other turbidite has a deviation of more than  $30^\circ$  at the 3140–3180 cm interval but for the rest, the dips in the inclination of  $K_3$  have an order of magnitude that is typical of turbidite currents composed of fine sands and silts (Park et al., 2013).

The difference in magnetic fabric between turbidite levels and hemipelagic sediment of Units 1 and 2 can be easily observed on the Jelinek (Pj/T) and Flinn (F/L) diagrams (Fig. 4). The T shape parameter indicates an oblate sedimentary fabric in most points from Units 1 and 2. Several samples, especially from turbidites, are characterized by T values that are close to zero and even negative indicating a triaxial to prolate type fabric. In Unit 2 which is supposedly associated with less turbidite activity, the lineation (L), foliation (F) and the corrected degree of anisotropy (Pj) have lower values than in Unit 1, but the turbidite sequences remain clearly distinguished. Fig. 4 also shows the Pj-Km and Pj-d50 diagram in order to investigate the influence of mineralogical and grain size in AMS. These diagrams didn't show a clear linear correlation between the highest degree of anisotropy values and the highest Km/d50 values. These results indicate that Pj values are not influenced by mineralogical/grain size variations and likely reflect changes in hydrodynamic conditions during turbidite deposition.

The stereographic plots of the principal  $K_1$  and  $K_3$  susceptibility axes

are shown in Fig. 5. The plots are divided into two types, turbidites and hemipelagic sediments, based on the median grain-size for Unit 1 and Ti/Ca ratios for Unit 2.

In Unit 1, The  $K_1$  axes are broadly girdle-distributed on the bedding plane, whereas the  $K_3$  axes are subvertical in almost all samples reflecting a well-developed sedimentary fabric. The  $K_1$  axes of Unit 2 present also girdle-distributed but with a weak clustering. The  $K_3$  axes are subvertical and slightly tilted towards the horizontal plane. This weak clustering could indicate a paleocurrent imprint. However, as the samples were not palaeomagnetically oriented, we cannot determinate absolute paleocurrent direction.

### 5.3. Low temperature SIRM

Low-temperature SIRM curves for three selected samples corresponding to Unit 1, Unit 2 and the turbidite located  $\sim 1733$  cm are shown in Fig. 6. All samples display a similar behavior which suggests that they share similar magnetic mineralogy. We note that the turbidite sample at 1733 cm has much higher SIRM values indicating that it was enriched in magnetic minerals.

A sharp Verwey transition at  $\sim 120$  K due to magnetite is present in both RT-SIRM and ZFC-FC curves of all samples. The RT-SIRM curves are characterized by a humped shape in both cooling and warming curves. The cooling curve shows first an increase that reaches a maximum at around  $175\text{--}200$  K, and then a strong decrease ahead the Verwey transition. Below 90 K, the remanence continues to slightly increase to 10 K. The RT-SIRM cooling and warming curves are reversible below 90 K. The total lost remanence after warming back at 300 K is between 6% for the turbidite at 1733 cm and 20% for sample at 830 cm (Unit 2). This behavior might suggest the presence of maghemite (Özdemir and Dunlop, 2010) or/and goethite (Taylor et al., 2014) but the RT-SIRM warming and cooling curves and their first derivatives (not shown) display a transition at circa 260 K which corresponds to the Morin transition of hematite (Özdemir et al., 2008).

Finally, in the FC-ZFC experiments both the FC and ZFC curves show a gradual loss of remanence during warming. The FC values lie between 30% and 60% above the ZFC values at 10 K. They remain well separated throughout the experiment and converge at 300 K. Similar behavior has been observed in loess and paleosols and suggest the presence of goethite (Taylor et al., 2014).

## 6. Discussion

### 6.1. Changes in deposition

The AMS results obtained in this study revealed a tight relationship between magnetic fabric and turbidite activity. As observed in Fig. 3 and Fig. 4, the turbidite sequences are characterized by a very high degree of anisotropy (Pj) and foliation (F) in both Units 1 and 2. The magnetic fabric shows also a higher lineation (L) and dips in the inclination of the  $K_3$  axes between  $15^\circ$  and  $25^\circ$  for several but no all turbidites (Fig. 3).

In order to better show the relationship between the magnetic fabric and the sedimentary structure, we have made a zoom on one of the thickest turbidites located in section 25 of core MD12-3417 between 3600 and 3670 cm depth which correspond to 3665–3749 cm of the composite depth (Fig. 7).

Downcore X-ray radiography makes it possible to distinguish changes in grain-size and sedimentary structures with lighter shade of grey levels corresponding to a coarse-grained turbidite sequence. This sequence is characterized by parallel sub-horizontal, cross laminations and oblique laminations. These structures were also observed in thin section of other coarse-grained turbidites and are cut by fluid escapes structures as convolute laminations or pillars, (Fournier et al., 2017).

Vertical variations in the magnetic fabric parameters reflect these changes in sedimentation conditions. Parameters Pj, L and Km show

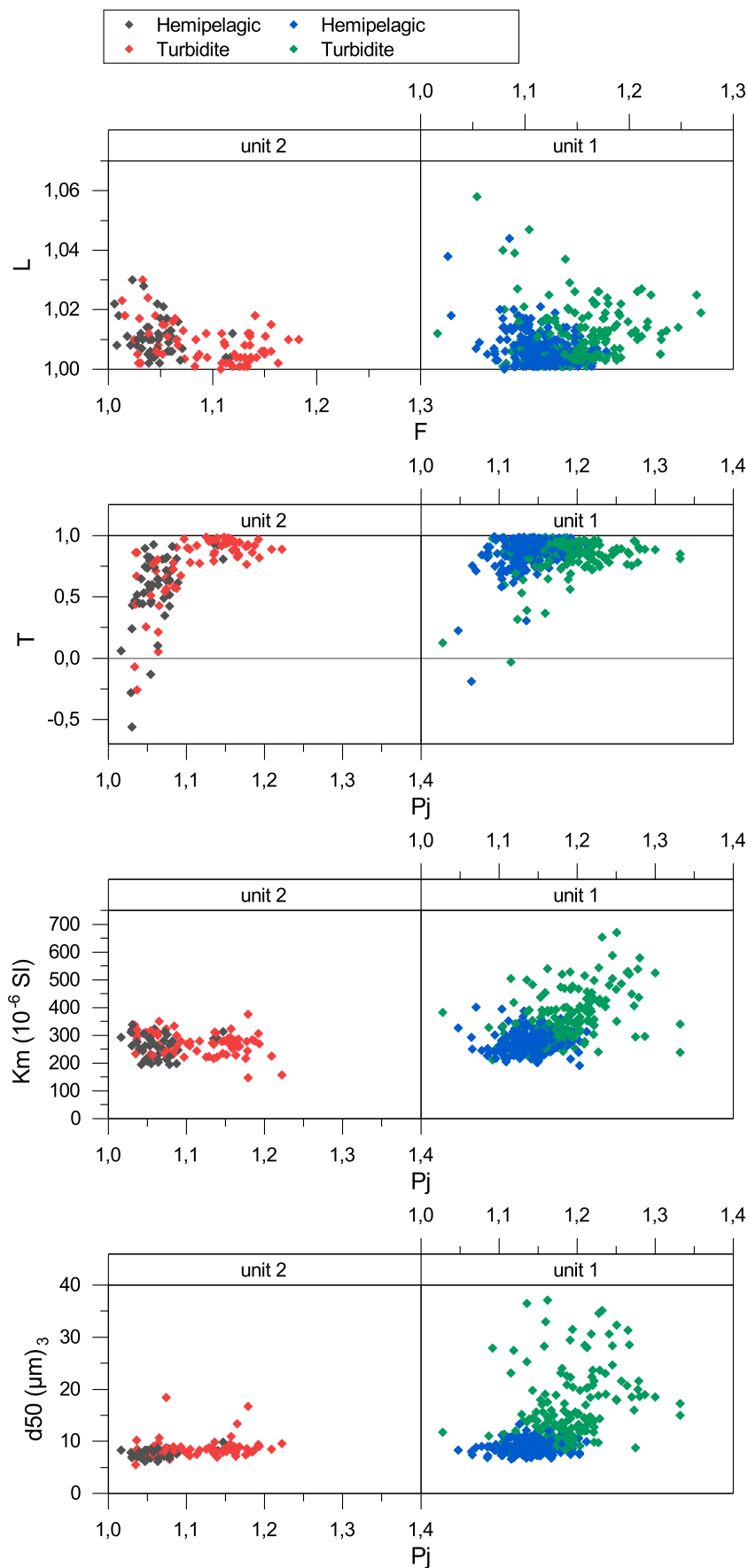
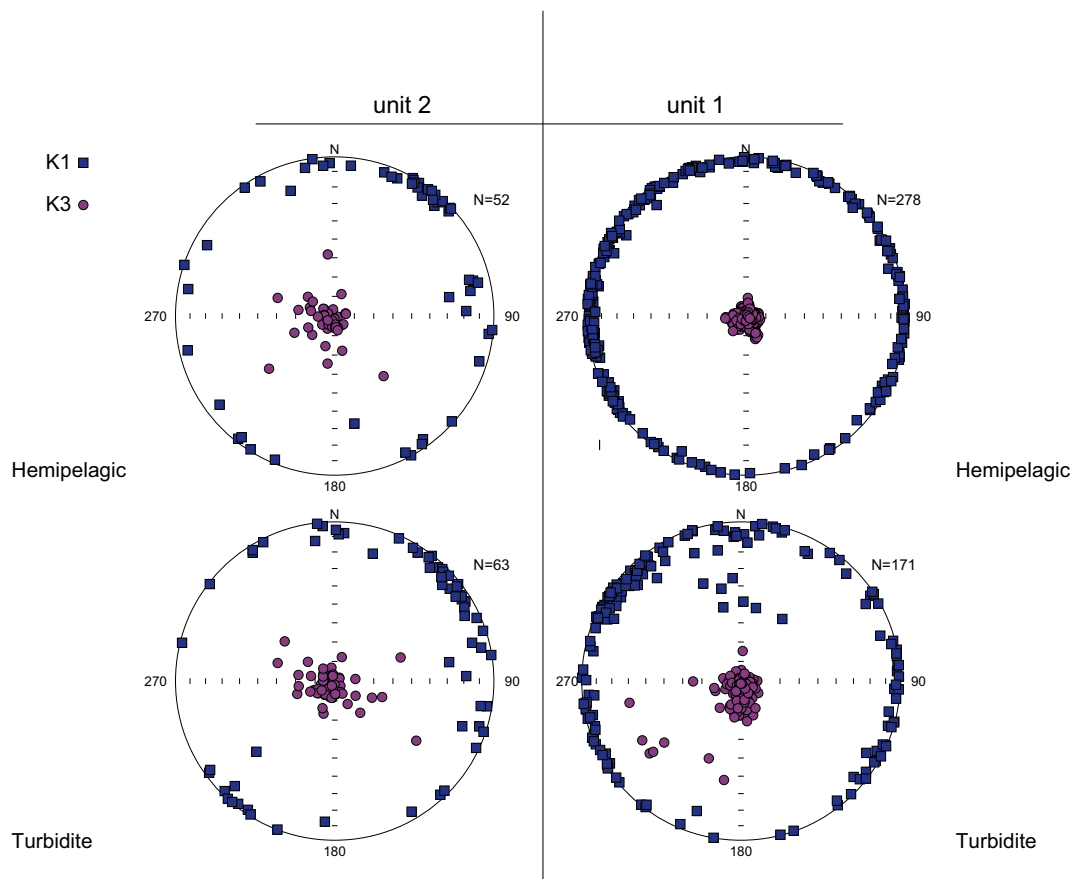


Fig. 4. : From top to the bottom Flinn diagrams (L/F); a) Pj/T diagram; Pj-Km and Pj-d50 diagrams of core MD17&18. Data from the disturbed section 11 were not plotted. Turbidites levels (T) were differentiated from the “hemipelagic” sediment in each Unit using d50 and Zr/Rb records in Unit 1 and ln(Ti/Ca) record in Unit 2;



**Fig. 5.** Stereoplots of principal axes orientations of the AMS ellipsoid in samples from Units 1 and 2. The plots are divided into two types, turbidites and hemipelagic sediments. Blue squares indicate  $K_1$  axes ( $K_{max}$ ) and pink circles indicate  $K_3$  axes ( $K_{min}$ ). The stereoplots are oriented to the the core generatrix and but not geographically oriented. (For interpretation of the references to colour in this figure legend, the reader is referred to the web version of this article.)

higher values in the turbidite sequences and  $\ln K_3$  shows deviations of up to  $20^\circ$  from vertical. It is interesting to note that the variations in AMS parameters are not necessarily in phase along the turbidite sequences and that  $L$ , although increasing, is still very low.

Thus, the most significant results are the unusually high levels of  $P_j$  and  $F$  in turbidites, both the coarse-grained turbidites from Unit 1 but also the fine-grained turbidites of Unit 2 (Fig. 4). These turbidites are terrigenous mainly composed by quartz, phyllosilicates (muscovite and clinocllore), detrital calcite and feldspars (Fig. S1).

The fluctuations in  $P_j$  and  $F$  could be explained by changes in grain-size and/or composition related to changes in depositional conditions, influx materials and or/in environmental changes.

However, as we mentioned above, even though the turbidites, especially the coarse-grained ones in Unit 1, have higher  $P_j$  values, there is no linear correlation between the  $P_j$  and  $K_m/d50$  values (Fig. 4). This is especially the case in Unit 2, where turbidite levels are fine-grained and  $K_m$  are relative low, and nevertheless,  $P_j$  values are much higher than hemipelagic sediments.

Besides, the high  $P_j$  values observed in our study could be explained by the presence of flattened phyllosilicates that are strongly anisotropic. Indeed, the selected samples measured by X-ray diffractometry (Fig. S1) indicates an important contribution of muscovite and clinocllore, a mineral of the chlorite family. The mean degree of anisotropy of these minerals is  $P_j = 1.15$  (Martín-Hernández and Hirt, 2003), in the range of the mean  $P_j$  values of Unit 2 but lower than the mean  $P_j$  values of Unit 1 (Fig. 4). Therefore, the presence of these minerals is not sufficient to explain the extremely high values of  $P_j$  observed in core MD17 & 18.

An alternative cause of this extremely high  $P_j$  values could be high

deposition rates. During consolidation, the weight of the sediment column, compress and compact the sediment. In hemipelagic sediments with relative low sedimentation rates, consolidation increase gradually with depth. With increasing vertical burial load at depth, clay mineral particles rotate to form horizontal face-to-face contacts, accompanied by simultaneous dewatering and porosity reduction. The effect of this process on the microstructure of the sediment is the formation of a fabric characterized by a well-defined horizontal foliation plane and strong degree of anisotropy (Kawamura and Ogawa, 2004; Maffione and Morris, 2017).

The sharp increase of the anisotropy degree in the turbidite sequences resembles the pattern expected for “apparent over-consolidation”, whereby the sediments appear more consolidated than expected by simple burial for a given depth, and therefore the degree of anisotropy is greater (Schwehr et al., 2006; Maffione and Morris, 2017). Furthermore, because turbidite sequences are deposited so quickly, they are free from the effects associated with bioturbation (Fig. 7 and Fig. S2, complementary data). Indeed, previous works have indicated that bioturbation can have effects in the AMS by scattering the direction of the principal susceptibilities axes (Ellwood, 1984; Bradák and Kovács, 2014).

The high sedimentation rate plays an important role in explaining the high  $P_j$  values observed in the MD17&18 core, although, as can be seen, the relationship between the degree of anisotropy and the sedimentation rate is not linear. According to the age model, the sedimentation rate decreases sharply at 2840 cm, from 9.5 cm/yr to 3.5 cm/yr, but this does not affect the  $P_j$  values. It should be remembered however that these sedimentation rates are exceptional in marine sediments and there may be a threshold effect. In addition,

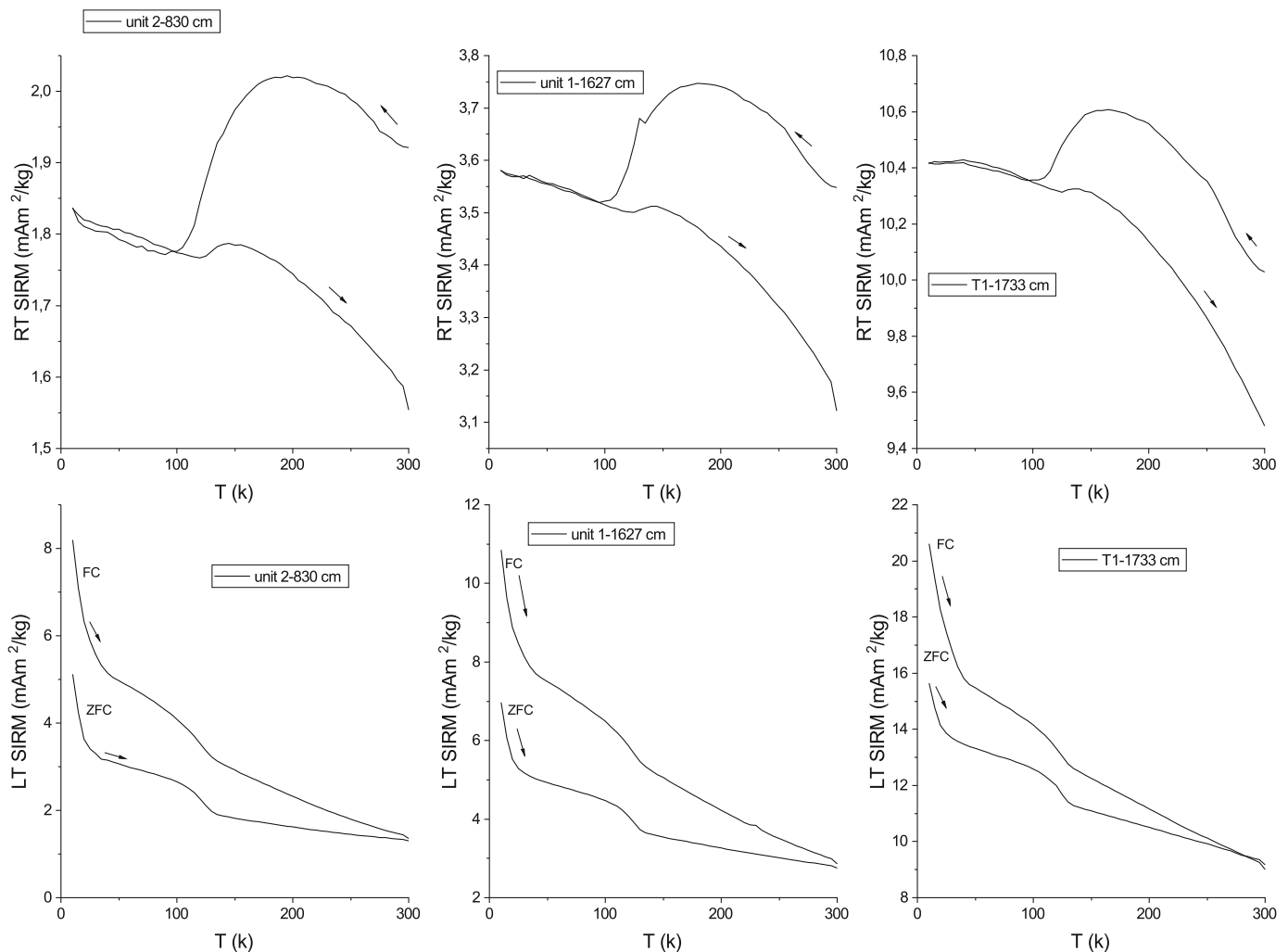


Fig. 6. RT-SIRM ZFC/FC curves for three selected samples at 830 cm (Unit 2); 1627 cm (Unit 1) and 1733 cm (turbidite layer T1 from Unit 1). The arrows mark the cooling or warming direction for each curve.

turbidites are instantaneous events and the deposition of each single turbidite pulse can be faster than the estimated average sedimentation rates.

Such high  $P_j$  and/or  $F$  values in turbidite sequences in marine sediments have been observed elsewhere in rapid sediments deposits, for example, sediments from Bermuda Rise, northern California (Joseph et al., 1998) and mass transport deposits (MTD) from Ursa Basin, northern Gulf of Mexico (Meissl et al., 2011). Besides, Tanty et al. (2016) investigated the AMS properties of four turbidites layers with different environmental conditions and different thickness. The results showed that the highest values in the degree of anisotropy were observed in the thickest turbidite (174 cm) in core MD98-2194 located in the Okinawa trough.

We have compared the  $P_j$  results from core MD17&18 with  $P_j$  values obtained in turbidites (Joseph et al., 1998), MTD (Meissl et al., 2011) and  $P_j$  values obtained from hemipelagic sediments with low sedimentation rates (Chen et al., 2017). Turbidites and MTD sediments have higher  $P_j$  than hemipelagic sediments, but the degree of anisotropy in core MD17&18 is by far strongest (Fig. 8) than in all the core samples.

This suggests that the increase in  $P_j$  during the turbidite sequences in core MD17&18 reflects a greater compaction of sedimentary structure probably due to very high sedimentation rates. MTD sediments also show strong  $P_j$  values that was interpreted as an additional compaction imposed by fast deposition (Meissl et al., 2011). Higher compaction

results in a flattening of the sedimentary magnetic fabric with the  $K_3$  axis becoming shorter and an increase in shape parameters such as  $P_j$  and  $F$ . It should also be considered that overlying the “compaction” effect, mineralogy and particle size changes play a secondary role.

## 6.2. Changes in sediment sources

The low-temperature measurements performed on selected samples indicated that the magnetic mineralogy is dominated by magnetite, hematite and goethite. These minerals commonly occur at concentrations less than 1% in sediments and are therefore difficult to determine using classical mineralogical techniques like X-ray diffraction (Zhang et al., 2007). Magnetite, hematite and goethite have been identified in a ~ 7 Ma old sedimentary sequence of the Bengal Fan using rock-magnetic properties (Abrajevitch et al., 2009). Magnetite is the most common magnetic mineral found in sediments. The strong correlation between  $K_m$  and sediment grain-size is indicative of its detrital origin, carried by the G-B river system, the main source of detrital sediments during the Holocene (Joussain et al., 2017; Lupker et al., 2013). However, although the  $K_m$  signal is mainly controlled by detrital inputs from the G-B system, the  $K_m$  signal can be also be influenced by diagenetic processes. Under anoxic conditions, iron oxides can be reduced by hydrogen sulfide ( $H_2S$ ) to form pyrite ( $FeS_2$ ) (Phillips et al., 2017; Liu et al., 2019a) resulting in decreased  $K_m$  values. A recent study indicates that this process can be regulated by major changes in

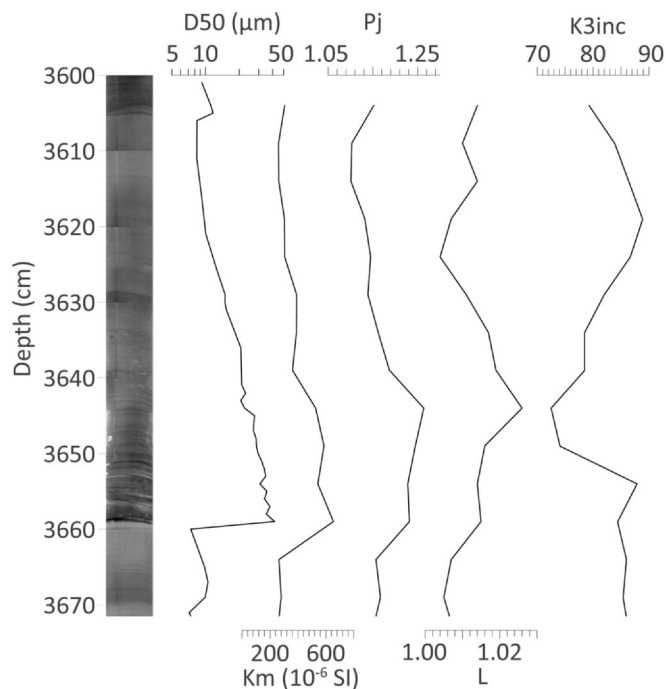


Fig. 7. Detailed results of the main AMS parameters presented in this study (Km, Pj, L et Inc. K<sub>3</sub>), the mean grain-size in µm (d50) and the R-X image obtained by scopix of one turbidite located in section 25 of core MD12-3417 between 3600 and 3670 cm (3665–3745 in composite depth).

sedimentation rate (Liu et al., 2019a) such as those observed in core MD17&18.

However, in a recent study based on sulphur speciation and isotope ratios of core MD161/29 (Volvoikar et al., 2020) collected near core MD17&18 (Fig. 1) no dominant influence of diagenesis on km values could be observed. As in the case of our study, the km values mainly reflect sediment inputs from the rivers G-B.

Due to its strong magnetic moment magnetite dominates Km, but goethite, hematite and phyllosilicates have also low to medium magnetic susceptibilities that can contribute to the global signal in presence of low magnetite concentration.

The turbidite sequences have higher Km values which indicates an increase in the concentration of magnetite and the Anhyseretic Remanent Magnetization (ARM) to magnetic susceptibility ratio (ARM/k) as well as the hysteresis parameters reveal an increase in the magnetite grain-size within the youngest coarse-grained turbidite located between 120 and 155 cm (Tanty et al., 2016). Similar results were found in other turbidite sequences from core MD17&18 (Moreno et al., 2014; Fig. S3, supplementary data). Summarizing the turbidite layers are characterized by higher terrigenous grain-size, higher magnetite concentration and higher magnetite grain-size.

A previous study (Suganuma et al., 2009) suggests that the input of magnetite in sediments from the Bengal Fan is controlled by the intensity of the Asian summer monsoon. Stronger monsoon yields a northwestward expansion of the area of precipitation in the Himalayas and the northern Indian subcontinent. This process generates an expansion of the soil area which increases the pedogenic activity in the G-B catchment area and in turn the input of magnetite in the Bengal Fan (Suganuma et al., 2009). The highest Km values occurred during Unit 1

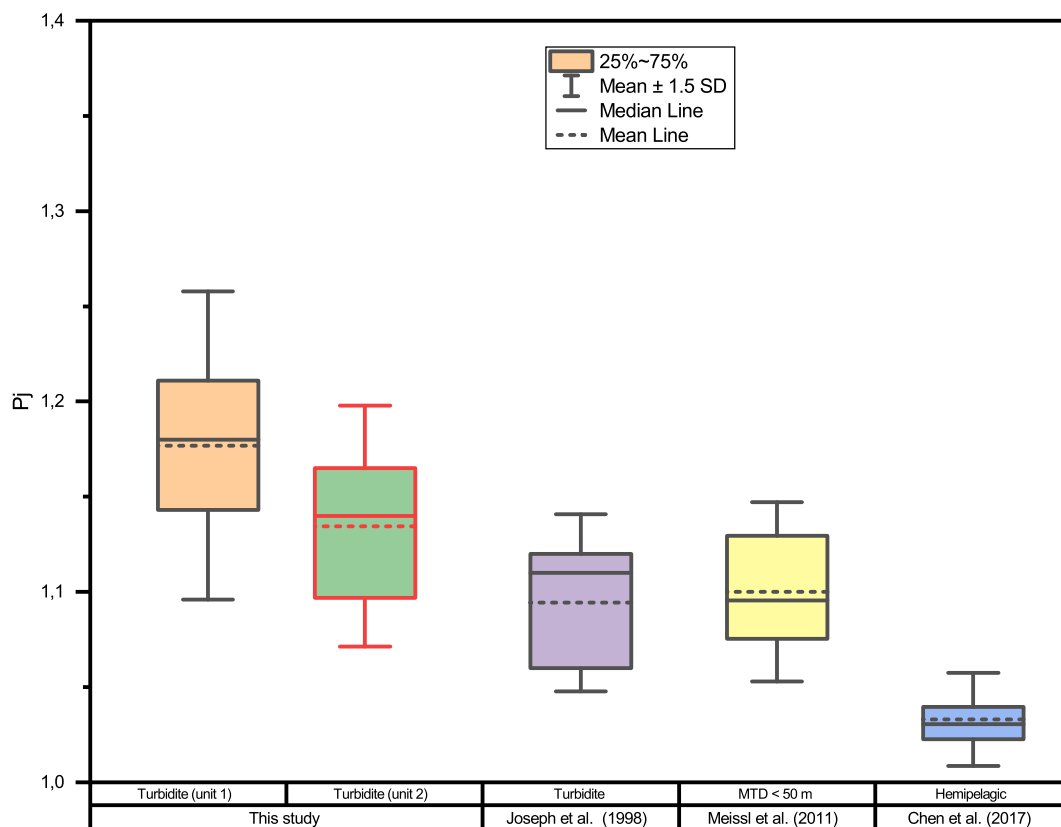


Fig. 8. Box charts displaying the mean, median and the first and third quartiles of Pj values from turbidites of Unit 1 (T1) and Unit 2 (T2) in the composite core MD17 & 18. Whiskers represent the standard deviation above and below the mean of the data ( ± 1.5SD). Results were compared to the results from the distal portion of the Delgada deep-sea fan off northern California containing thin turbidite sand and silt layers (Joseph et al., 1998); samples of muddy levee sediments from Ursa Basin located on the northern Gulf of Mexico containing mass transport deposits (MTD) (Meissl et al., 2011) and samples of terrigenous sediments deposited in the South China Sea during the Pleistocene (Chen et al., 2017). In all cases, the samples depths are less than 50 m.

at the beginning of the Holocene, when monsoon intensity was at its highest. Similar results were observed in the clay assemblage and the chemical weathering proxies of MD17&18 sediments reconstructed from major element concentrations (Joussain et al., 2017). This study demonstrated that the input of detrital material from the highlands was more important during the early-middle Holocene (9.8–6 ka cal. BP) whereas they mainly originated from the Indo-Gangetic plain thereafter.

## 7. Conclusions

The magnetic fabric of the turbidite sequences in core MD17&18 is mainly characterized by an increase in the Pj parameter. This increase occurs not only in the coarse-grained turbidites of Unit 1, but also in the fine turbidites of Unit 2, hardly recognizable in the grain-size parameters. The Pj values were extremely high (1.028–1.332) in Unit 1 between 9.8 and 9.2 ka cal. BP. During these 600 years, almost 30 m of sediment was accumulated and the turbidite activity was almost continuous. The average Pj values slightly decreased after 9.2 ka cal. BP in Unit 2 (1016–1222) associated to an abrupt shift in sedimentation rate. Despite this decrease, the sedimentation rate (0.02–0.18 cm/year) and the Pj values are still very high in comparison with hemipelagic sediments.

We propose that this increase in Pj is due to the exceptional sedimentation rate observed in core MD17&18, which can reach up to 9.5 cm/yr in Unit 1 causing an additional compaction effect, however, changes in particle size and mineralogy can play a secondary role.

Besides, magnetic mineralogy reveals that the magnetic minerals representative of the Ganges and Brahmaputra drainage area are magnetite, hematite and goethite. The Km record represents the fluctuations in the concentration of magnetite concentration and indicates higher supply of magnetite in Unit 1 when the turbidite activity was the most important.

The difference in Km values between early and late Holocene suggest a modification of the sources of fluvial sediments within the Ganges-Brahmaputra catchment basin (highlands versus floodplain) related to changes in the intensity of the Asian summer monsoon. During early Holocene, stronger monsoon yields a northwestward expansion of the area of precipitation in the Himalayas and the northern Indian subcontinent leading to a higher contribution of highlands sediments. Conversely, after 6 ka cal. BP, the detrital material mainly originated from the floodplain. These results are in agreement with previous work on core MD17&18 based on strontium and neodymium isotopic signatures (Joussain et al., 2017).

Our study shows that the use of AMS properties enables the identification of turbidite layers even when these are difficult to recognize using the classical technics based on grain-size and/or XRF analysis. Therefore, the AMS technique has a strong potential for the interpretation of changes in deposition regimes associated with climate or environmental changes.

Supplementary data to this article can be found online at <https://doi.org/10.1016/j.margeo.2020.106347>.

## Declaration of competing interest

The authors declare that they have no known competing financial interests or personal relationships that could have appeared to influence the work reported in this paper.

## Acknowledgements

This work was supported by the *Agence Nationale de la Recherche* project MONOPOL (grant ANR-11-BS56-0024). MONOPOL cruise aboard the Marion-Dufresne was supported by the IPEV, and the crew is acknowledged for its help. We are also grateful to MNHN and ISTeP

technicians for their help during sampling and laboratory preparation: Lola Johannes, Ravi Daliah and Florence Savignac. We are grateful for the comments and suggestions from two anonymous reviewers for suggestions and to improve the manuscript.

## References

- Abdeldayem, A.L., 1999. Magnetic susceptibility anisotropy and remanence of some deep-sea sediments of the Tokai basin. In: Yuasa, M. (Ed.), *Marine Geological Investigations of the Tokai Offshore Area*. Geological Survey. Japan Cruise Report, vol. 24. pp. 127–146.
- Abrajewitch, A., der Voo, R.V., Rea, D.K., 2009. Variations in relative abundances of goethite and hematite in Bengal Fan sediments: climatic vs. diagenetic signals. *Mar. Geol.* 267, 191–206.
- Banerjee, S.K., King, J., Marvin, J., 1981. A rapid method for magnetic granulometry with applications to environmental studies. *Geophys. Res. Lett.* 8, 333–336.
- Bassinot, F., Beaufort, L., 2012. MD 191/MONOPOL cruise. RV Marion Dufresne. <https://doi.org/10.17600/12200050>.
- Baudin, F., Disnar, J.-R., Aboussou, A., Savignac, F., 2015. Guidelines for Rock-Eval analysis of recent marine sediments. *Org. Geochem.* 86, 71–80.
- Beckers, A., Beck, C., Hubert-Ferrari, A., Tripanas, E., Crouzet, C., Sakellariou, D., Papatheodorou, G., De Batist, M., 2016. Influence of bottom currents on the sedimentary processes at the western tip of the Gulf of Corinth, Greece. *Mar. Geol.* 378, 312–332.
- Boyle, J.F., Chiverrell, R.C., Schillereff, D.N., 2015. Approaches to Water Content Correction and Calibration for  $\mu$ XRF Core Scanning: Comparing X-Ray Scattering with Simple Regression of Elemental Concentrations.
- Bradák, B., Kovács, J., 2014. Quaternary surface processes indicated by the magnetic fabric of undisturbed, reworked and fine-layered loess in Hungary. *Quat. Int.* 319, 76–87.
- Calvert, S.E., Price, N.B., 1983. Geochemistry of namibian shelf sediments. In: Suess, E., Thiede, J. (Eds.), *Coastal Upwelling and its Sediment Record*. NATO Conference Series (IV Marine Sciences), vol 10B Springer, Boston, MA.
- Campos, C., Beck, C., Crouzet, C., Demory, F., Van Welden, A., Eris, K., 2013. Deciphering hemipelagites from homogenites through anisotropy of magnetic susceptibility. Paleoseismic implications (Sea of Marmara and Gulf of Corinth). *Sediment. Geol.* 292, 1–14.
- Campos, C., Beck, C., Crouzet, C., Carrillo, E., Van Welden, A., Tripanas, E., 2014. Late Quaternary paleoseismic sedimentary archive from deep central Gulf of Corinth: time distribution of inferred earthquake-induced layers. *Ann. Geophys.* 56.
- Carrillo, E., Beck, C., Audemard, F.A., Moreno, E., Ollarves, R., 2008. Disentangling Late Quaternary climatic and seismo-tectonic controls on Lake Mucubají sedimentation (Mérida Andes, Venezuela). *Palaeogeogr. Palaeoclimatol. Palaeoecol.* 259, 284–300.
- Chen, Q., Kissel, C., Liu, Z., 2017. Late Quaternary climatic forcing on the terrigenous supply in the northern South China Sea: input from magnetic studies. *Earth Planet. Sci. Lett.* 471, 160–171.
- Curry, J.R., Emmel, F.J., Moore, D.G., 2003. The Bengal Fan: morphology, geometry, stratigraphy, history and processes. *Mar. Pet. Geol.* 19, 1191–1223.
- Dypvik, H., Harris, N.B., 2001. Geochemical facies analysis of fine-grained siliciclastics using Th/U, Zr/Rb and (Zr + Rb)/Sr ratios. *Chem. Geol.* 181, 131–146.
- Ellwood, B.B., 1984. Bioturbation; minimal effects on the magnetic fabric of some natural and experimental sediments. *Earth Planet. Sci. Lett.* 67, 367–376.
- Fauquembergue, K., Fournier, L., Zaragosi, S., Bassinot, F., Kissel, C., Malaizé, B., Caley, T., Moreno, E., Bachelery, P., 2019. Factors controlling frequency of turbidites in the Bengal fan during the last 248 kyr cal BP: clues from a presently inactive channel. *Mar. Geol.* 415 105965.
- Felletti, F., Dall'Olivo, E., Muttoni, G., 2016. Determining flow directions in turbidites: an integrated sedimentological and magnetic fabric study of the Miocene Marnoso Arenacea Formation (northern Apennines, Italy). *Sediment. Geol.* 335, 197–215.
- Fournier, L., Fauquembergue, K., Zaragosi, S., Zorzi, C., Malaizé, B., Bassinot, F., Joussain, R., Colin, C., Moreno, E., Leparmentier, F., 2017. The Bengal fan: External controls on the Holocene Active Channel turbidite activity. *The Holocene* 27 (6), 900–913.
- Ge, S., Shi, X., Liu, Y., Wang, K., Zou, J., Diao, J., Zhu, Z., Wang, C., 2012. Turbidite and bottom-current evolution revealed by anisotropy of magnetic susceptibility of redox sediments in the Ulleung Basin, Sea of Japan. *Chin. Sci. Bull.* 57, 660–672.
- Goodbred, S.L.J., Kuehl, S.A., 2000. Enormous Ganges-Brahmaputra sediment discharge during strengthened early Holocene monsoon. *Geology* 28, 1083.
- Gupta, A.K., Das, M., Anderson, D.M., 2005. Solar influence on the Indian summer monsoon during the Holocene. *Geophys. Res. Lett.* 32 L17703\_1-L17703\_4.
- Joseph, L.H., Rea, D.K., Pluijm, B.A.v.d., 1998. Use of grain size and magnetic fabric analyses to distinguish among depositional environments. *Paleoceanography* 13, 491–501.
- Joussain, R., Liu, Z., Colin, C., Duchamp-Alphonse, S., Yu, Z., Moréno, E., Fournier, L., Zaragosi, S., Dapigny, A., Meynadier, L., Bassinot, F., 2017. Link between Indian monsoon rainfall and physical erosion in the Himalayan system during the Holocene. *Geochem. Geophys. Geosyst.* 18, 3452–3469.
- Kawamura, K., Ogawa, Y., 2004. Progressive change of pelagic clay microstructure during burial process: examples from piston cores and ODP cores. *Mar. Geol.* 207, 131–144.
- King, J.W., Banerjee, S.K., Marvin, J., Ozdemir, O., 1982. A comparison of different magnetic methods for determining the relative grain-size of magnetite in natural materials: some results from lake sediments. *Earth Planet. Sci. Lett.* 59, 404–419.
- Kissel, C., Laj, C., Lehman, B., Labyrie, L., Bout-Roumaizelles, V., 1997. Changes in the strength of the Iceland-Scotland Overflow Water in the last 200,000 years: evidence

- from magnetic anisotropy analysis of core SU90-33. *Earth Planet. Sci. Lett.* 152, 25–36.
- Kissel, C., Laj, C., Mazaud, A., Dokken, T., 1998. Magnetic anisotropy and environmental changes in two sedimentary cores from the Norwegian Sea and the North Atlantic. *Earth Planet. Sci. Lett.* 164, 617–626.
- Kolla, V., Bandyopadhyay, A., Gupta, P., Mukherjee, B., Ramana, D.V., 2012. Morphology and internal structure of a recent upper bengal fan-valley complex. In: Prather, B.E., Deptuck, M.E., Mohrig, D., Hoorn, B.V., Wynn, R.B. (Eds.), *Application of the Principles of Seismic Geomorphology to Continental Slope and Base-of-Slope Systems: Case Studies from SeaFloor and Near-Sea Floor Analogues*. SEPM Society for Sedimentary Geology p. 347–369.
- Kuhnt, W., Holbourn, A., Xu, J., Opdyke, B., Deckker, P., Röhl, U., Mudelsee, W., 2015. Southern hemisphere control on Australian monsoon variability during the late deglaciation and Holocene. *Nat. Commun.* 6, 5916.
- Kumar, K., Agrawal, S., Sharma, A., Pandey, S., 2019. Indian summer monsoon variability and vegetation changes in the core monsoon zone, India, during the Holocene: a multiproxy study. *The Holocene* 29, 110–119.
- Lambeck, K., Rouby, H., Purcell, A., Sun, Y., Sambridge, M., 2014. Sea level and global ice volumes from the Last Glacial Maximum to the Holocene. *Proc. Natl. Acad. Sci.* 111, 15296–15303.
- Liu, X., Rendle-Bühning, R., Henrich, R., 2018. High-and low-latitude forcing of the East African climate since the LGM: inferred from the elemental composition of marine sediments off Tanzania. *Quat. Sci. Rev.* 196, 124–136.
- Liu, X., Fike, D., Li, A., Dong, J., Xu, F., Zhuang, G., Rendle-Bühning, R., Wan, S., 2019a. Pyrite sulfur isotopes constrained by sedimentation rates: evidence from sediments on the East China Sea inner shelf since the late Pleistocene. *Chem. Geol.* 505, 66–75.
- Liu, J., He, W., Cao, L., Zhu, Z., Xiang, R., Li, T., Shi, X., Liu, S., 2019b. Staged fine-grained sediment supply from the Himalayas to the Bengal Fan in response to climate change over the past 50,000 years. *Quat. Sci. Rev.* 212, 164–177.
- Lupker, M., France-Lanord, C., Galy, V., Lavé, J., Kudrass, H., 2013. Increasing chemical weathering in the Himalayan system since the Last Glacial Maximum. *Earth Planet. Sci. Lett.* 365, 243–252.
- Maffione, M., Morris, A., 2017. The onset of fabric development in deep marine sediments. *Earth Planet. Sci. Lett.* 474, 32–39.
- Martín-Hernández, F., Hirt, A.M., 2003. The anisotropy of magnetic susceptibility in biotite, muscovite and chlorite single crystals. *Tectonophysics* 367, 13–28.
- Meissl, S., Behrmann, J.H., Franke, C., 2011. Magnetic fabrics in Quaternary sediments, Ursa Basin, northern Gulf of Mexico record transport processes, compaction and submarine slumping. *Mar. Geol.* 286, 51–64.
- Migeon, S., Weber, O., Faugeres, J.C., Saint-Paul, J., 1998. SCOPIX: a new X-ray imaging system for core analysis. *Geo-Mar. Lett.* 18, 251–255.
- Milliman, J.D., 2001. River inputs. In: Steele, J.H., Turekian, K.K., Thorpe, S.A. (Eds.), *Encyclopedia of Ocean Sciences*. Elsevier, pp. 2419–2427.
- Moreno, E., Marty, G., Fournier, L., Zaragosi, S., Fauquembergue, K., Bassinot, F., Garidel-Thoron, T., Valet, J.-P., 2014. Magnetic Properties of Marine Sediments from the Bengal fan: Record of Climatic Changes during Holocene and Turbiditic Activity from the River System, Castle Meeting: New Trends on Paleo. Rock and Environmental Magnetism, Evora (Portugal).
- Özdemir, Ö., Dunlop, D.J., 2010. Hallmarks of maghemitization in low-temperature remanence cycling of partially oxidized magnetite nanoparticles. *J. Geophys. Res. Solid Earth* 115, 148–227.
- Özdemir, Ö., Dunlop, D.J., Berquó, T.S., 2008. Morin transition in hematite: size dependence and thermal hysteresis. *Geochem. Geophys. Geosyst.* 9.
- Parés, J.M., Hassold, N.J.C., Rea, D.K., van der Pluijm, B.A., 2007. Paleocurrent directions from paleomagnetic reorientation of magnetic fabrics in deep-sea sediments at the Antarctic Peninsula Pacific margin (ODP Sites 1095, 1101). *Mar. Geol.* 242, 261–269.
- Park, M.E., Cho, H., Son, M., Sohn, Y.K., 2013. Depositional processes, paleoflow patterns, and evolution of a Miocene gravelly fan-delta system in SE Korea constrained by anisotropy of magnetic susceptibility analysis of interbedded mudrocks. *Mar. Pet. Geol.* 48, 206–223.
- Phillips, S.C., Johnson, J.E., Clyde, W.C., Setera, J.B., Maxbauer, D.P., Severmann, S., Riedinger, N., 2017. Rock magnetic and geochemical evidence for authigenic magnetite formation via iron reduction in coal-bearing sediments offshore Shimokita Peninsula, Japan (IODP Site C0020). *Geochem. Geophys. Geosyst.* 18, 2076–2098.
- Revel, M., Ducassou, E., Skonieczny, C., Colin, C., Bastian, L., Bosch, D., Migeon, S., Mascle, J., 2015. 20,000 years of Nile River dynamics and environmental changes in the Nile catchment area as inferred from Nile upper continental slope sediments. *Quat. Sci. Rev.* 130, 200–221.
- Schwehr, K., Tauxe, L., Driscoll, N., Lee, H., 2006. Detecting compaction disequilibrium with anisotropy of magnetic susceptibility. *Geochem. Geophys. Geosyst.* 7.
- Schwenk, T., Spieß, V., Hübscher, C., Breitzke, M., 2003. Frequent channel avulsions within the active channel-levee system of the middle Bengal Fan—an exceptional channel-levee development derived from Parasound and Hydrosweep data. *Deep-Sea Res. II Top. Stud. Oceanogr.* 50, 1023–1045.
- Sharma, S., Joachimski, M., Sharma, M., Tobschall, H.J., Singh, I.B., Sharma, C., Chauhan, M.S., Morgenroth, G., 2004. Lateglacial and Holocene environmental changes in Ganga plain, Northern India. *Quat. Sci. Rev.* 23, 145–159.
- St-Onge, G., Mulder, T., Francus, P., Long, B., 2007. Chapter two continuous physical properties of cored marine sediments. In: Hillaire-Marcel, C., De Vernal, A. (Eds.), *Developments in Marine Geology*. Elsevier, pp. 63–98.
- Suganuma, Y., Yamazaki, T., Kanamatsu, T., 2009. South Asian monsoon variability during the past 800 kyr revealed by rock magnetic proxies. *Quat. Sci. Rev.* 28, 926–938.
- Sun, X., Liu, S., Li, J., Zhang, H., Zhu, A., Cao, P., Chen, M.-T., Zhao, G., Khokiatiwong, S., Kornkanitnan, N., Shi, X., 2019. Major and trace element compositions of surface sediments from the lower Bengal Fan: implications for provenance discrimination and sedimentary environment. *J. Asian Earth Sci.* 184, 104000.
- Tamaki, M., Suzuki, K., Fujii, T., 2015. Paleocurrent analysis of Pleistocene turbidite sediments in the forearc basin inferred from anisotropy of magnetic susceptibility and paleomagnetic data at the gas hydrate production test site in the eastern Nankai Trough. *Mar. Pet. Geol.* 66, 404–417.
- Tantý, C., Valet, J.-P., Carlu, J., Bassinot, F., Zaragosi, S., 2016. Acquisition of detrital magnetization in four turbidites. *Geochem. Geophys. Geosyst.* 17, 3207–3223.
- Tarling, D.H., Hroudá, F., 1993. *The Magnetic Anisotropy of Rocks*, 1 ed. Chapman & Hall.
- Taylor, S.N., Lagroix, F., Rousseau, D., Antoine, P., 2014. Mineral magnetic characterization of the Upper Pleniglacial Nussloch loess sequence (Germany): an insight into local environmental processes. *Geophys. J. Int.* 199, 1463–1480.
- Thamban, M., Kawahata, H., Rao, V.P., 2007. Indian summer monsoon variability during the Holocene as recorded in sediments of the Arabian Sea: timing and implications. *J. Oceanogr.* 63, 1009–1020.
- Thomas, B.L., Cutler, M., Novak, C., 2012. A modified counterconditioning procedure prevents the renewal of conditioned fear in rats. *Learn. Motiv.* 43, 24–34.
- Thu, M.K., Tokuyama, H., Murayama, M., Party, K.H.s., 2001. HINDOO cruise deep-sea channel survey in the Bay of Bengal. *地質学雑誌* 107 XIX-XX.
- Tjallingii, R., Röhl, U., Kölling, M., Bickert, T., 2007. Influence of the water content on X-ray fluorescence core-scanning measurements in soft marine sediments. *Geochem. Geophys. Geosyst.* 8.
- Unger, D., Ittekkot, V., Schäfer, P., Tiemann, J., Reschke, S., 2003. Seasonality and interannual variability of particle fluxes to the deep Bay of Bengal: influence of riverine input and oceanographic processes. *Deep-Sea Res. II Top. Stud. Oceanogr.* 50, 897–923.
- Volvoikar, S., Mazumdar, A., Peketi, A., Dewangan, P., Sawant, B., Manaskanya, A., Goswami, H., Das, D., Pujari, S., 2020. Contrasting sulfidization in the turbidite and hemipelagic sediments of Bengal Fan. *Mar. Pet. Geol.* 118, 104408.
- Weber, M.E., Wiedicke, M.H., Kudrass, H.R., Hübscher, C., Erlenkeuser, H., 1997. Active growth of the Bengal Fan during sea-level rise and highstand. *Geology* 25, 315–318.
- Weber, M.E., Wiedicke-Hombach, M., Kudrass, H.R., Erlenkeuser, H., 2003. Bengal Fan sediment transport activity and response to climate forcing inferred from sediment physical properties. *Sediment. Geol.* 155, 361–381.
- Weltje, G.J., Tjallingii, R., 2008. Calibration of XRF core scanners for quantitative geochemical logging of sediment cores: theory and application. *Earth Planet. Sci. Lett.* 274, 423.
- Zhang, Y.G., Ji, J., Balsam, W.L., Liu, L., Chen, J., 2007. High resolution hematite and goethite records from ODP 1143, South China Sea: co-evolution of monsoonal precipitation and El Niño over the past 600,000 years. *Earth Planet. Sci. Lett.* 264, 136–150.